The International Journal of Advanced Manufacturing Technology (2018) 96:4367–4379
https://doi.org/10.1007/s00170-018-1906-0

ORIGINAL ARTICLE

Investigations on femtosecond laser-modified microgroove-textured cemented carbide YT15 turning tool with promotion in cutting performance

Ding Ye[1,2] · Yang Lijun[1,2] · Cheng Bai[1] · Wang Xiaoli[1] · Wang Yang[1,2] · Xie Hui[1,2]

Received: 22 October 2017 / Accepted: 14 March 2018 / Published online: 25 March 2018

Abstract
This work puts forward femtosecond laser modification of microgroove textures on a rake face of the cemented carbide YT15 turning tool in order to promote its cutting performance. Technological tests focusing on femtosecond laser ablation of YT15 are established with purpose of obtaining the impacts of machining parameters, like pulse energy, scanning velocity, and scanning times on the morphology of microgrooves, mechanism of which are analyzed from multiple aspects. Cylindrical turning tests and numerical simulations by ABAQUS based on orthogonal cutting model and Johnson-Cook (J-C) constitutive model are carried out to investigate the variation of cutting performance applying non-textured (NT), parallel grooves textured (PGT), and vertical grooves textured (VGT) turning tools. Matlab is utilized to filter the force signal collected by a three-dimensional piezoelectric dynamometer. Both theoretical and experimental results demonstrate that parallel grooves with specific dimension parameters on a rake face of a turning tool can improve cutting performance more significantly with less tool wear.

Keywords Femtosecond laser modification · Microgroove textures · YT15 turning tool · Cutting performance

1 Introduction

Textures on a solid surface make it possible for the control of specific tribological, optical, and mechanical properties [1]. In terms of tribology, a low-friction surface can be manufactured by applying textures on it owing to the generation of hydrodynamic pressure, storage of the lubricants, and chips [2]. In the turning process, cutting force and friction on the tool-chip interface, which cause plastic deformation of the substrate as well as tool wear, are the dominant factors that determine cutting performance of turning tools [3].

The introduction of textures has been made possible by the development of micro- and nanomachining technologies, such as surface shot peening [4], micro EDM micro EDM-assisted with high-frequency vibration [5], reactive-ion etching [6], pulsed air arc treatment (PAAT) [7], and laser surface texturing (LST) [8–9]. Among these techniques, LST has several characteristics; these include, but are not limited to, well-processing flexibility, high-machining repeatability and accuracy, and lack of tool wear. Moreover, comparing with conventional long-pulse laser, femtosecond laser has ultrashort pulse duration and ultrahigh peak power density, which is beneficial for restraining thermal diffusion effectively. Lei et al. realized surface texturing of cutting inserts with microholes by means of femtosecond laser micromachining without affecting the performance of the inserts. Their finite analysis indicated that micropool lubrication brings minimum amount of lubricant into the chip–tool interface and improves the severe contact conditions by reducing the coefficient of friction [10]. Deng et al. carried out dry cutting tests on femtosecond laser textured rake face of WC/TiC/Co carbide tools. They suggested that the deposition of lubricating film on the textured rake face is an effective way to improve the cutting performance of conventional carbide tools in dry cutting [11]. Kümmel et al. found out that adhesion behavior of built-up edges can be reduced by applying channel textures fabricated by femtosecond laser, which resulted in higher wear rates of the cutting tool and simultaneously in a slightly better surface

✉ Yang Lijun
dy1992hit@163.com

[1] School of Mechatronics Engineering, Harbin Institute of Technology, Harbin 150001, China

[2] Key Laboratory of Micro-systems and Micro-structures Manufacturing, Ministry of Education, Harbin Institute of Technology, Harbin 150001, China

quality of the machined workpiece, due to less built-up edges formation. In addition, by applying a channel texture, the wear was increasing [12]. Wang et al. employed Ti-Sapphire femtosecond laser to produce textured surfaces with different microgroove spacing and inclination angles on surface of AISI304L steel. Experimental results verified that femtosecond laser surface texturing has marked potential to reduce friction coefficient and wear rate comparing with untextured surface. Meanwhile, the microgroove inclination angles had influence on the friction behavior of textured surface to a certain extent [13].

In view of the results of literature review, there are scarcities of detailed investigations on ablation characteristic and manufacturing craft of specific microtextures on the turning tool by femtosecond laser as well as researches on chip morphology and tool wear. In current work, parallel and vertical grooves are designed on the rake face of the cemented carbide YT15 turning tool. Follow-up technological experiments are established to explore optimized parameter group for modifying microgrooves, in which influence rules of multiple femtosecond laser machining variables on morphology of microgrooves are detailed analyzed. Cylindrical turning tests and numerical simulations by ABAQUS based on orthogonal cutting model and Johnson-Cook (J-C) constitutive model are carried out to investigate the cutting performance variation, including cutting force, friction coefficient, chips morphology, and tool wear, by applying NT, PGT, and VGT turning tools. A corresponding analysis, targeting at role of textures playing in the turning process, are put forward.

2 Analytical model and experimental setup

2.1 Analytical model setup

Figure 1a, c schematically illustrates a cylindrical turning model and its two-dimensional view. In the interface of the rake face of the turning tool and substrate, chips are fiberized and flow along the rake face. To investigate the cutting performance of the microgrooves' textured turning tool and chips morphology in detail, orthogonal cutting model is utilized to characterize the cutting process as the representative elemental volume of cylindrical turning, schematic diagram, and force analysis of which are shown in Fig. 1b, d, where F_r is total cutting force; F_f is friction; F_n is normal force on chips; F_x is back force; F_y is tangential component force; a_p is cutting depth; β is frictional angle; γ_0 is rake angle; t_0 is the thickness of an undeformed chip thickness; and t_c is chip thickness. S, T, and C represent substrates, turning tools, and chips respectively.

Specifically, F_r in Fig. 1d is analyzed from two aspects. The first aspect is relative to flow direction of chips. F_f is parallel to flow direction of chips while F_n is perpendicular to it. The other aspect is relative to moving direction of the turning tool. F_y is parallel to moving direction of the turning tool while F_x is perpendicular to it. Therefore, Eqs. (1)–(2) can be realized, where μ is friction coefficient between the turning tool and substrate.

$$\mu = \tan\beta = \frac{F_f}{F_n} \tag{1}$$

$$\tan(\beta - \gamma_0) = \frac{F_x}{F_y} \tag{2}$$

Microgrooves in different directions are designed on the rake face of the turning tool. Surface and cross-sectional morphologies are illustrated in Fig. 2, in which parallel grooves means its direction is perpendicular to flow direction of chips [14]. The finite element (FE) model is established in the circumstance of ABAQUS. Finer mesh is used in the interface of the turning tool and substrate to ensure the accuracy of simulation, as indicated in Fig. 3. Displacement and velocity constraint are imposed on the bottom of substrate. The turning tool moves at constant velocity v.

The Johnson-Cook (J-C) constitutive model is employed to describe variation of temperature, stress, and strain rate of bulk material during turning and mathematical expression of which is written in Eq. (3) [15].

$$\sigma = [A + B\varepsilon^n]\left[1 + C\ln\frac{\dot{\varepsilon}}{\dot{\varepsilon}_0}\right]\left[1 - \left(\frac{T - T_{\text{mom}}}{T_{\text{melt}} - T_{\text{mom}}}\right)^m\right] \tag{3}$$

where A is initial yield stress; B is strain hardening modulus; n is hardening exponent; C is strain rate; m is thermal-softening exponent; and T, T_{mom} and T_{melt} are current temperature, room temperature, and melting temperature respectively; ε and $\dot{\varepsilon}$ are equivalent plastic strain and reference strain rate. Applied parameters concerning a C45 steel substrate is shown in Tab. 1. Average friction coefficient between turning tool and substrate in the simulation refers to the experimental measured value. Moreover, a chip separation criterion based on shear failure is introduced into the analytical model, which provides a more practical basis for simulations [16].

2.2 Experimental setup

A femtosecond diode-pumped mode-locked pulsed solid state Yb: KGW laser (Pharos) with a maximum average laser power of 15 W, a wavelength of 1030 nm, pulse duration of 255 fs, and repetition frequency from 1 Hz to 1.1 MHz is applied to produce microtextures on the rake face of the turning tool. Experimental light path is shown in Fig. 4. The output beam is linear-polarized. Laser beam diameter $2\omega_0$ at $\frac{1}{e^2}$ intensity level is diffraction limited and is related to the laser and focusing lens parameters, as written in Eq. (4), according to Yang et al. [17].

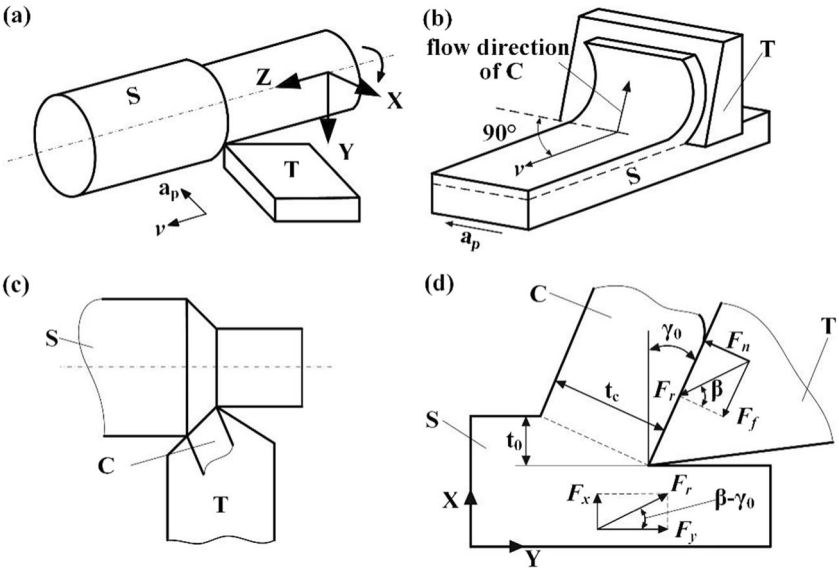

Fig. 1 **a** Cylindrical turning and **c** its two-dimensional view; **b** orthogonal cutting and **d** its force analysis

$$2\omega_0 = \frac{4\cdot\lambda\cdot f}{\pi\cdot d}\cdot M^2 \tag{4}$$

where λ is the laser wavelength, which value is 1030 nm; f is the focal length of the focusing lens, which value is 75 mm; d is the beam diameter at the focusing lens, which value is 5 mm after being expanded by beam expander. M^2 is the Gaussian beam quality in TEM_{00} mode, which value is 1.13 according to factory test report of Pharos. Hence, laser beam diameter $2\omega_0$ in this work is estimated to be 25.12 μm.

The cemented carbide YT15 turning tool employed in this work is provided by the Zhuzhou Cemented Carbide Group Co., Ltd: physical properties and geometric parameters of which are shown in Tables 2 and 3. Hard phases of the turning tool are WC and TiC, while the adhesive is Co. Mass fraction of these elements are 79, 15, and 6% respectively.

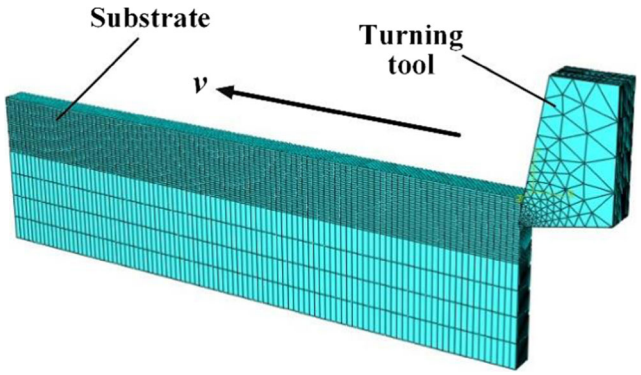

Fig. 3 Mesh setup in ABAQUS

After femtosecond laser processing, the turning tool is ultrasonic cleaned in ethanol for 5 min. The surface morphology

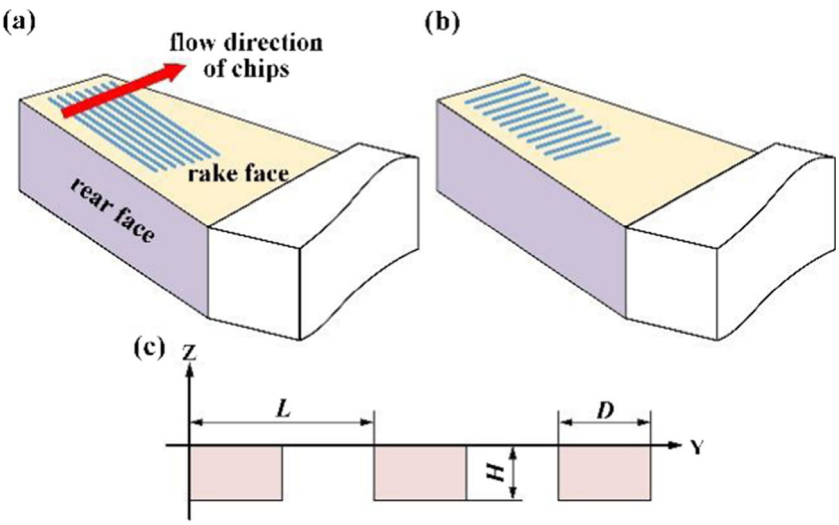

Fig. 2 Characterization of **a** PGT, **b** VGT, and **c** cross-sectional parameters

Table 1 Applied parameters of C45 steel in J-C model

Parameter	A/MPa	B/MPa	C	m	n	T_{melt}/°C
Value	507	320	0.28	1.06	0.064	1492

and internal structure of microtextures are characterized by a digital microscope with a large depth of field microscope (VHX5000).

Cylindrical turning tests are established on numerical control lathe (BRT5085i) with a maximum gyration diameter of 500 mm. Cutting force is measured by a three-dimensional piezoelectric dynamometer (YDC-III89A). An experimental system is shown in Fig. 5. The substrate applied in the turning experiments is C45 steel: physical properties of which are shown in Table 4.

During the turning tests, F_x, F_y, and F_z can be detected by the three-dimensional piezoelectric dynamometer. However, during the tests, some factors like vibration of lathe contribute to the disturbance of detected force signals. Therefore, the original data are filtered employing Matlab in this work. The example of comparison between original F_y and filtered F_y is shown in Fig. 6.

Considering the rake angle γ_0 of the employed turning tool is 25°, the experimental friction coefficient between the turning tool and substrate can be obtained based on Eqs. (1)–(2), written as Eq. (5).

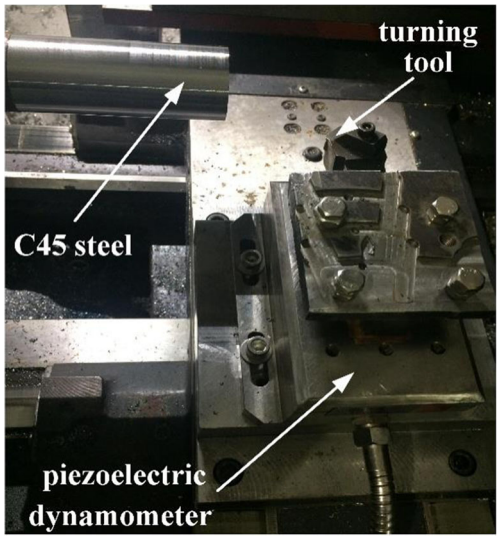

Fig. 5 Cylindrical turning tests system

$$\mu = tan\left[tan^{-1}\left(\frac{F_x}{F_y}\right) + 25^{\circ}\right] \tag{5}$$

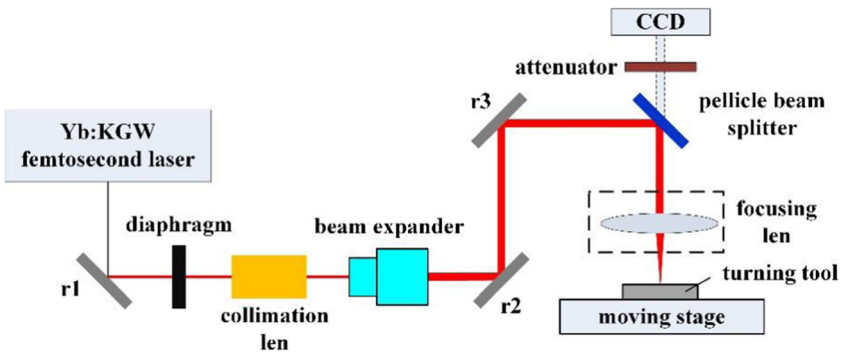

Fig. 4 Schematic diagram of experimental light path

Table 2 Physical properties of the cemented carbide YT15 turning tool

Density ρ/g cm^{-3}	Young modulus E/GPa	Poisson's ratio v	Thermal conductivity λ/ W · m^{-1} ∘ C^{-1}	specific heat capacity C/J $kg^{-1}K^{-1}$	Linear expansion coefficient $\alpha/10^{-6}$ K
11.6	550	0.23	33.5	251.2	6.5

Table 3 Geometric parameters of the cemented carbide YT15 turning tool

Dimension/mm	Rake angle γ_0/°	Relief angle α_0/°	Cutting edge angle κ_r /°	Cutting edge inclination λ_s/°	Cutting edge radius r/mm
16 × 16	25	− 11	45	0	0.4

Table 4 Physical properties of C45 steel

Density ρ g cm^{-3}	Young modulus E GPa	Poisson's ratio v	Thermal conductivity λ W $m^{-1} \circ C^{-1}$	Specific heat capacity C J $kg^{-1}K^{-1}$	Linear expansion coefficient α 10^{-6} K
7.85	210	0.31	38.13	524	13.09

3 Technological tests for modification of microgrooves

Specific dimensional parameters of microgrooves are listed in Table 5, which refers to the investigations put forward by Kawasegi N et al... [18]. According to Wang et al, a laser fluence characterizes groove width and depth most remarkably [19]. While the relationship between the laser fluence F and pulse energy E_p can be written as Eq. (6). Thus, the influences of pulse energy on groove morphology are investigated, results of which are shown in Fig. 7. Pulse frequency f, scanning time η, and scanning velocity v are set as 100 kHz, 1 and 1 mm/s respectively. Obviously, the increase of pulse energy yields the continuous increase in groove width and depth. At low pulse energy, there is no trace of debris around groove, as shown in Fig. 8a. While at high pulse energy level, thermal and mechanical effects induced by femtosecond laser pulse are significant and similar to those of long-pulse laser at high pulse energy. Heat affected zone (HAZ) as well as recast layer are observed in the surface, as shown in Fig. 8b.

$$F = \frac{2E_p}{\pi\omega_0{}^2} \tag{6}$$

Besides, the ablation depth of the material at a given pulse energy is determined by the effective pulse numbers N_{eff} and ablation rate L until reaching a saturation value due to pulse incubation effect [20]. Definition of N_{eff} and L are written as Eqs. (7) and (8), where λ and $F_{\text{th}}{}^{\lambda}$ are heat diffusion length and strong ablation threshold respectively. With a certain pulse energy, $F_{\text{th}}{}^{\lambda}$ is fixed. In this condition, ablation depth is determined by scanning velocity and scanning times under multiple scanning theoretically. Figures 9 and 10 demonstrate the effect of scanning velocity and scanning times on groove morphology.

Table 5 Dimensional parameters of micro grooves

Groove spacing/μm	Groove depth/μm	Groove width/μm
75/100/150	10/20/30	30/50/70

$$N_{\text{eff}} = \sqrt{\frac{\pi}{2}} \cdot \frac{2\omega_0 f}{v} \tag{7}$$

$$L = \lambda \cdot \ln \frac{F}{F_{th}{}^{\lambda}} \tag{8}$$

It is noticeable in Figs. 7, 9 and 10 that groove width and depth both varied significantly with pulse energy rather than scanning times and velocity. Hence, two different scanning strategies are applied in order to further discover proper processing techniques for designed grooves. Schematic diagrams of different scanning trace and corresponding groove

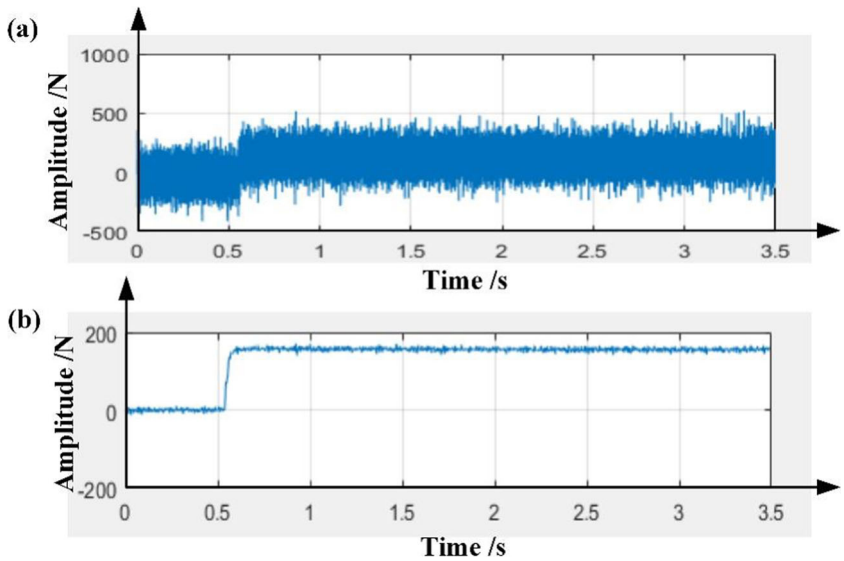

Fig. 6 Comparison of **a** original F_y signal and **b** filtered F_y signal

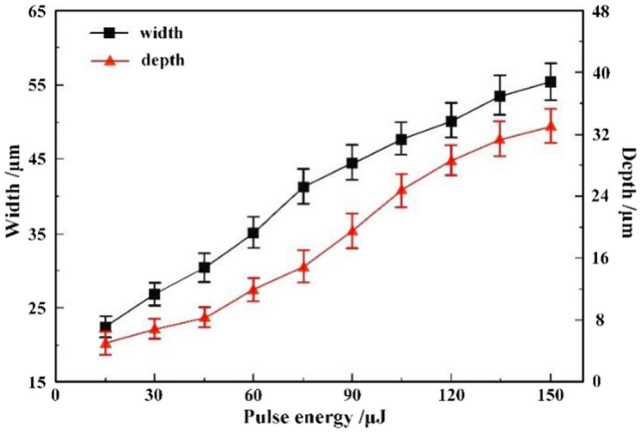

Fig. 7 Dependence of groove width and depth on pulse energy

morphologies are shown in Fig. 11. The comparison between Fig. 11b, d indicates that high pulse energy with less scanning times yields an inverse Gaussian-shaped groove, while low pulse energy with more scanning times yields a flat-bottom-shaped groove. Therefore, the latter scanning strategy is more appropriate for the fabrication of microgroove textures.

4 Results and discussions

4.1 Different microtextures

Stress nephogram is a reasonable approach to display the stress distribution of the model employed in ABAQUS [21, 22]. In this section, cutting velocity and cutting depth in both simulations and experiments are set as 120 m/min and 0.5 mm. Feed value in cylindrical turning tests is set as 0.1 mm/r. Mises stress nephograms on rake and rear surface of the turning tool with different textures in simulations are illustrated in Fig. 12, in which L, D, and H are set as 100, 50, and 20 μm respectively. It is obvious that stress mainly concentrates on the cutting edge of

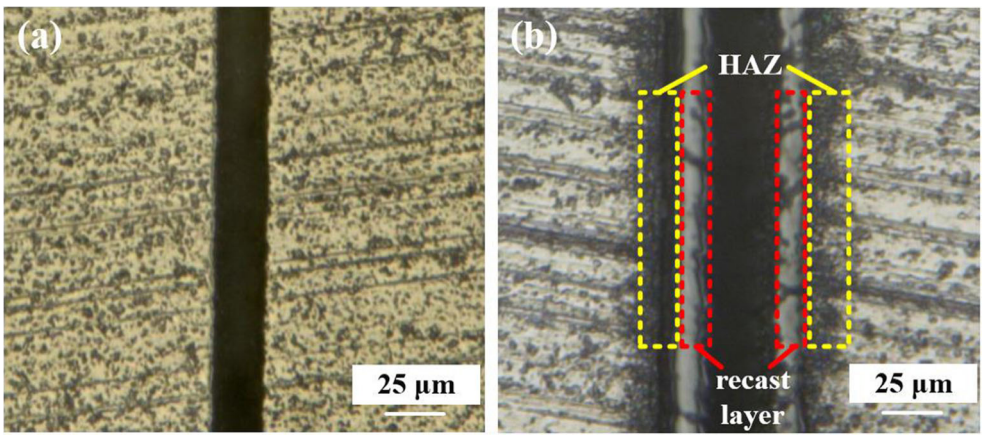

Fig. 8 Groove surface morphology under pulse energy of **a** 15 and **b** 150 μJ

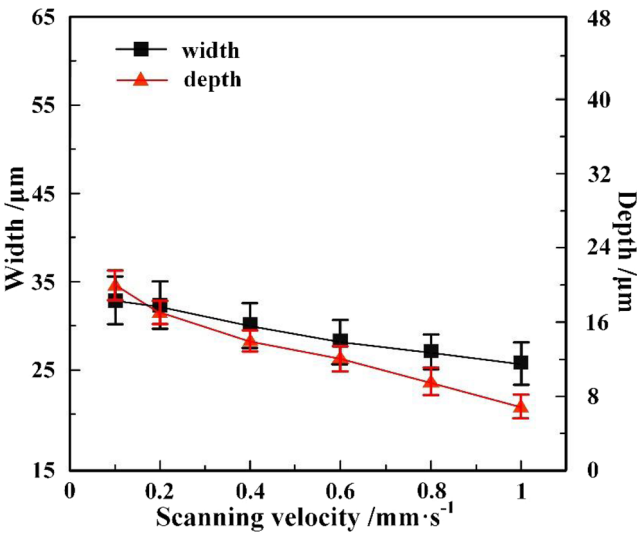

Fig. 9 Dependence of groove width and depth on scanning velocity. f, E_p, and η are 100 kHz, 30 μJ, 1

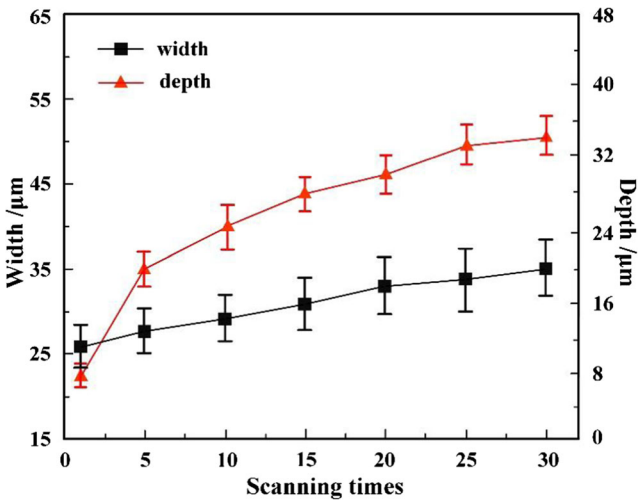

Fig. 10 Dependence of groove width and depth on scanning times. f, E_p, and v are 100 kHz, 30 μJ, 1 mm/s

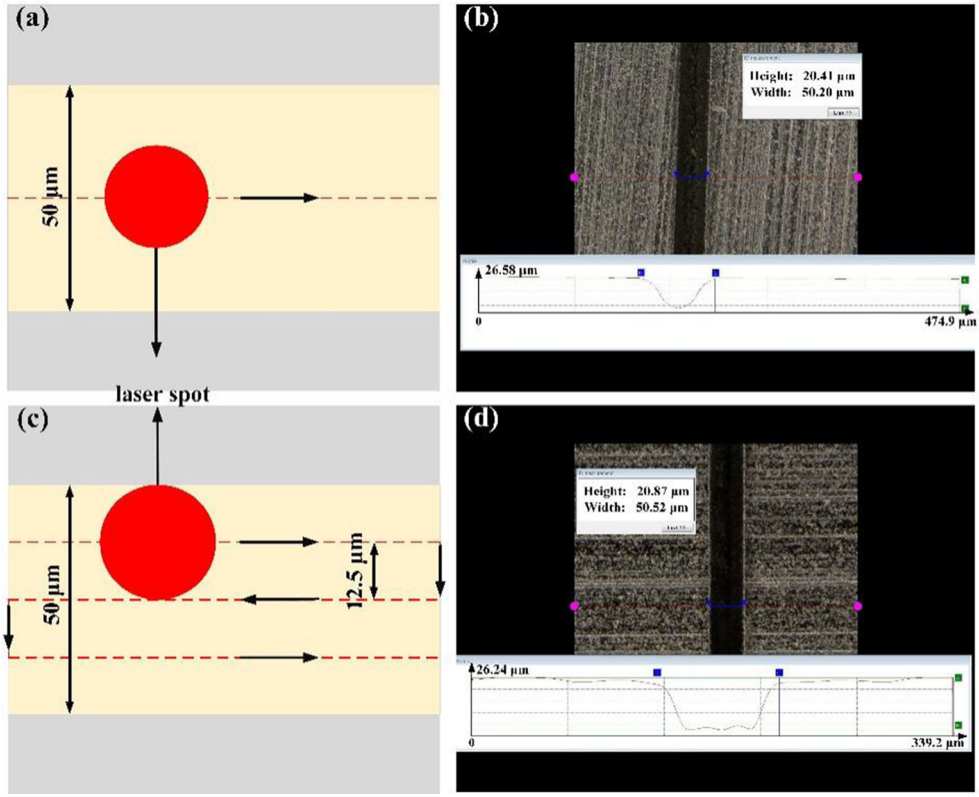

Fig. 11 **a** Linear scanning trace and **b** grooves morphologies, f, E_p, v, and η are 100 kHz, 90 μJ, 1 mm/s, 1; **c** multiple scanning trace and **d** grooves morphologies, f, E_p, v, and η are 100 kHz, 30 μJ, 1 mm/s, 5

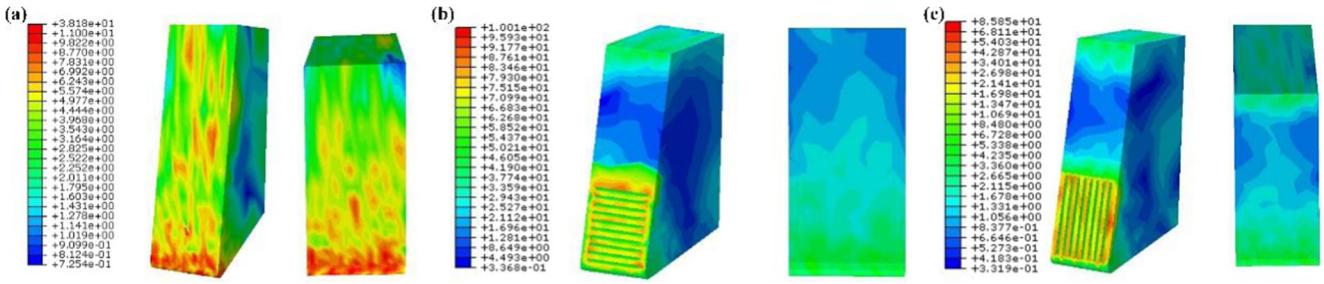

Fig. 12 Mises stress nephograms on rake and rear surface of **a** non-textures (NT), b PGT, **c** VGT turning tools

untextured turning tool. While with the existence of microtextures, stress turns out to be a more uniform distribution among the rake face.

Cutting performances of turning tools with different surface morphologies are varied. Relevant simulations and experiments are carried out, from which key parameters under

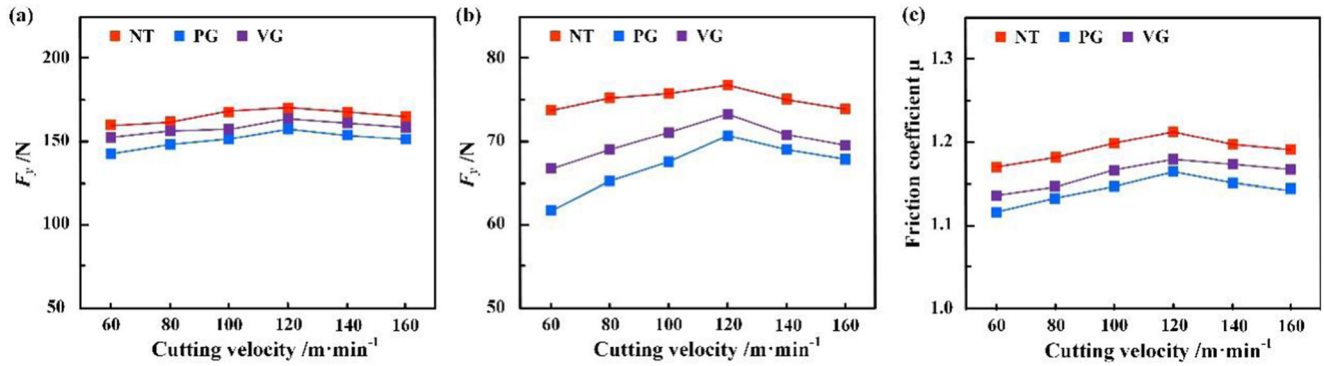

Fig. 13 Variation of experimental F_x, F_y, and friction coefficient μ under different cutting velocity

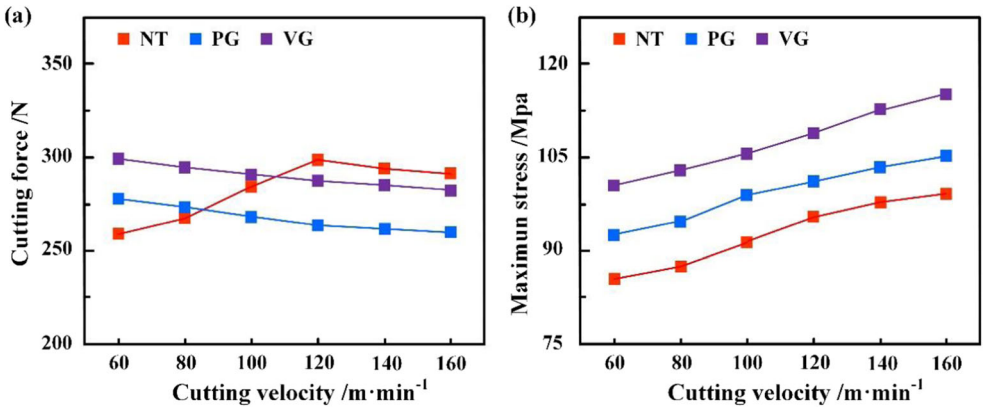

Fig. 14 Variation of theoretical average cutting force and maximum stress under different cutting velocity

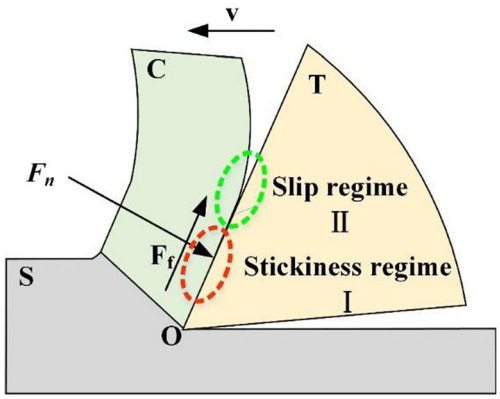

Fig. 15 Distribution of slip regime and stickiness regime

different cutting velocity are extracted, as shown in Figs. 13 and 14. F_z is not plotted in Fig. 13 as well as Figs. 18, 19, 20 in that it has tiny relationship with the comparison of cutting performance using different textured turning tools, which results in the difference between the theoretical cutting force and experimental joint cutting force (F_x and F_y). It is interesting to note that the average cutting force and friction coefficient for PGT and NGT turning tools experience noticeable decrease comparing with NT turning tools under higher cutting velocity rather than lower cutting velocity: both theoretically and experimentally. Analysis goes that contact region between rake face and substrate can be separated into slip regime and stickiness regime, as shown in Fig. 15. In stickiness regime, chips and the turning tool are in close contact with each other, which give birth to high processing temperature [23]. The interaction between the turning tool and substrate in this regime can be considered as a friction pair reasonably. Referring to the research of Pettersson et al., microtextures work as reservoirs for cutting liquid [2]. Under high processing temperature, cutting liquid reserved in the textures will expand upward, as illustrated in Fig. 16a. When the cutting liquid fully occupies textures, it will be brought into the gap between the substrate and turning tool, owing to the flow of chips. Correspondingly, a lubrication film is formed above textured regions, as illustrated in Fig. 16b. With the flow of chips and cutting liquid, net-increased pressure perpendicularly, upward to substrates, and comes into being in this progress, which characterizes the "secondary lubrication" effect differing from the lubrication effect induced by cutting liquid directly, as illustrated in Fig. 16b [24]. Net-increased pressure can balance the cutting force to some extent. The existence of microgrooves also results in the decrease the bond area between the turning tool and

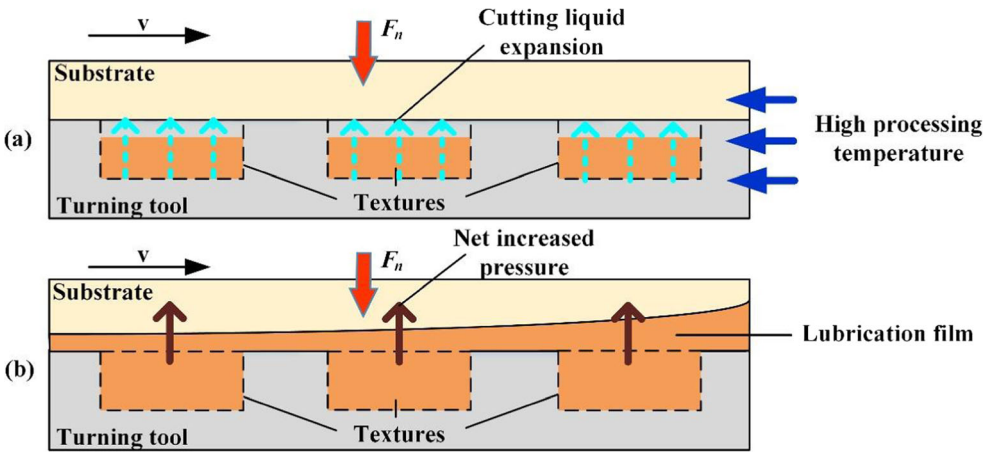

Fig. 16 Schematic diagram of **a** original state of friction pair **b** generation of lubrication film and net increased pressure

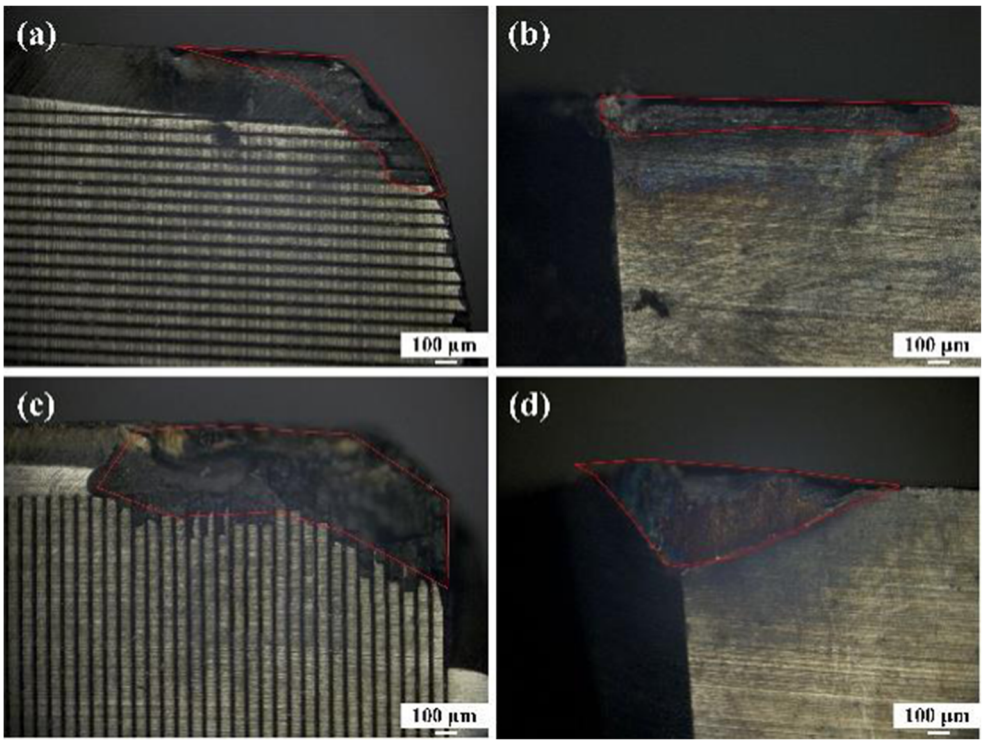

Fig. 17 Wear morphology of the rake and rear surface of **a, b** the PGT and **c, d** VGT turning tools

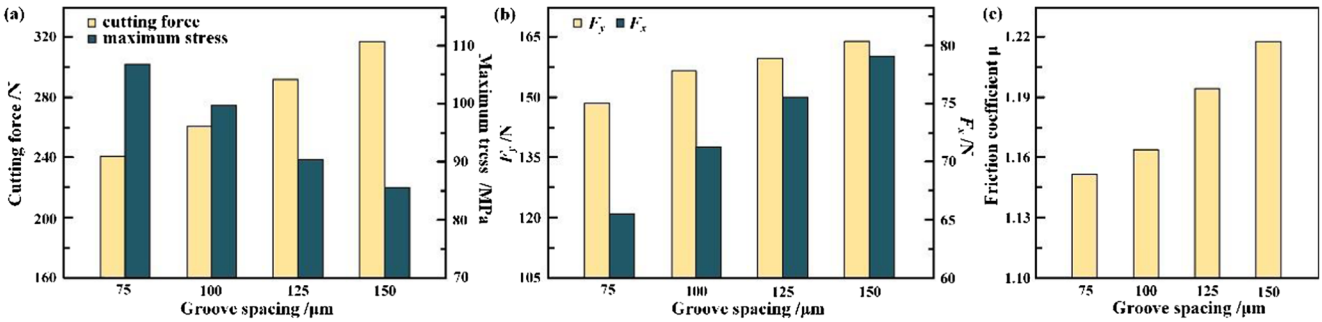

Fig. 18 Variation of **a** theoretical cutting force and maximum stress, **b** experimental F_y and F_x, **c** friction coefficient μ under different groove spacing

substrate, and this can weaken bond friction in the stickiness regime [25]. Both of these effects lead to lower cutting force and lower friction coefficient.

Another phenomenon discovered from Figs. 13 and 14 is the better cutting performance of the PGT turning tool comparing with the VGT turning tool. It is suggested that during

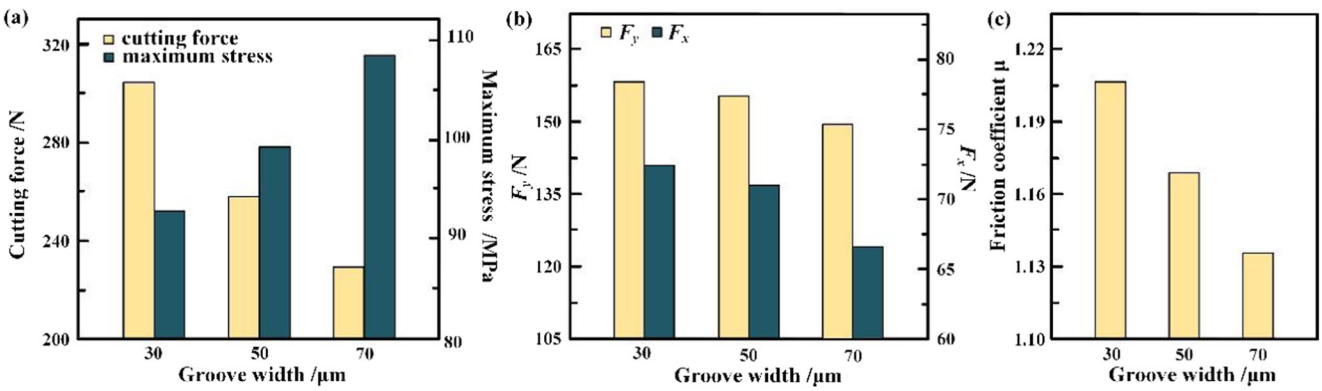

Fig. 19 Variation of **a** theoretical cutting force and maximum stress, **b** experimental F_y and F_x, **c** friction coefficient μ under different groove width

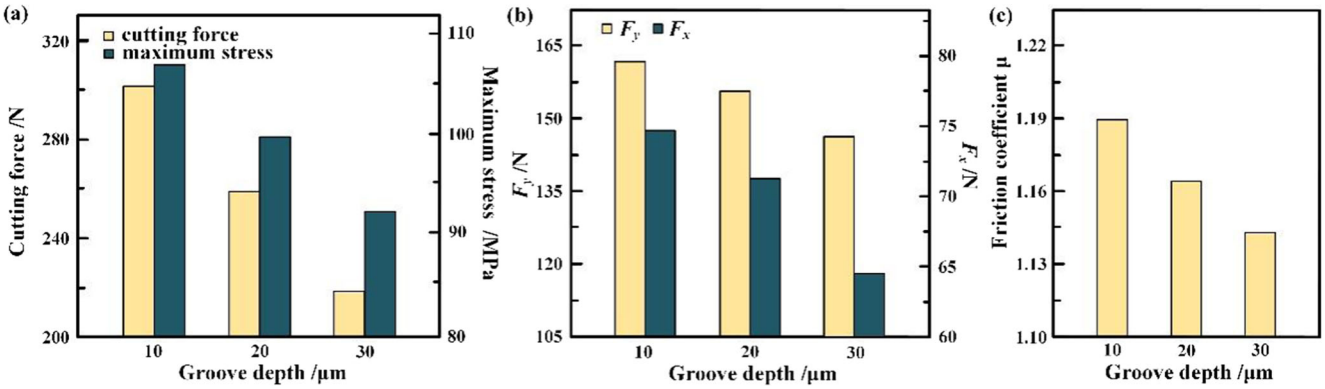

Fig. 20 Variation of **a** theoretical cutting force and maximum stress, **b** experimental F_y and F_x, **c** friction coefficient μ under different groove depth

turning experiment, chips will flow along vertical grooves. That is to say, cutting liquid continues to leak from instead of spread among the cutting region, which suppresses the formation of lubrication film and weakening the "secondary lubrication" effect.

Nevertheless, the improvement of cutting performance is accompanied by the increase of maximum stress according to the simulations. Figure 17 demonstrates the tool wear morphology of the PGT and VGT turning tool with the L, D, and H of 100, 50, and 20 μm under the working condition mentioned above. It is obvious that the wear mainly concentrates on the knifepoint, which is the focus of cutting stress referring to the simulations in Figs. 21, 22, 23 (see in Section 4.2). In addition, the VGT turning tool experiences much more severe wear comparing with the PGT turning tool, which attributes to the larger cutting force and higher friction coefficient as well as cutting stress.

By comparing cutting performance and wear of these turning tools, the PGT turning tool is better, and it will be the focus of researches in the following section.

4.2 Different dimensional parameter

Figures 18, 19, and 20 demonstrate variation of key physical properties under different groove array dimensions from aspects of simulations and experiments. In these figures, experimental data are firstly extracted and analyzed. And then, the experimental friction coefficients under different cutting condition are applied in the simulation process. Cutting velocity, cutting depth, and feed value are set as 120 m/min, 0.5 mm, and 0.1 mm/r. Standard parameters for L, D, and H are 100, 50, and 20 μm respectively.

Referring to Fig. 2, increasing groove spacing and decreasing groove width equal to the decrease of occupancy ratio of textures on rake face, the effect of which on cutting performance can be analyzed from three aspects. Firstly, as mentioned in Section 4.1, the interaction between the turning tool and substrate in the stickiness regime can be considered as a friction pair. Contact pressure intensity σ_c for a single texture can be calculated employing Hertz formula, written as Eq. (9) [26].

$$\sigma_c = \frac{1}{\pi}\sqrt{6 \cdot F_n \cdot \left(\frac{{}^{1}/_{\rho}}{\frac{1-\mu_1{}^2}{E_1}+\frac{1-\mu_2{}^2}{E_2}}\right)} \tag{9}$$

where F_n is imposed load. ρ is synthetical curvature radius of contact pair, $\frac{1}{\rho}=\frac{1}{\rho}+\frac{1}{\rho}$, where ρ_1 and ρ_2 are the radius of

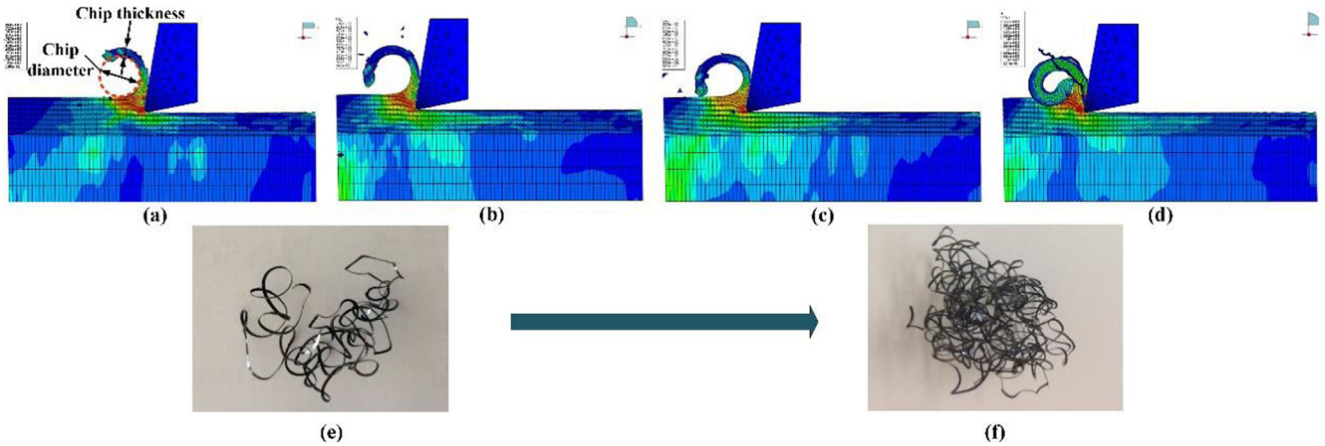

Fig. 21 Variation of chips morphology under different groove spacing **a**, **e** 75; **b** 100; **c** 125; **d**, **f** 150 μm

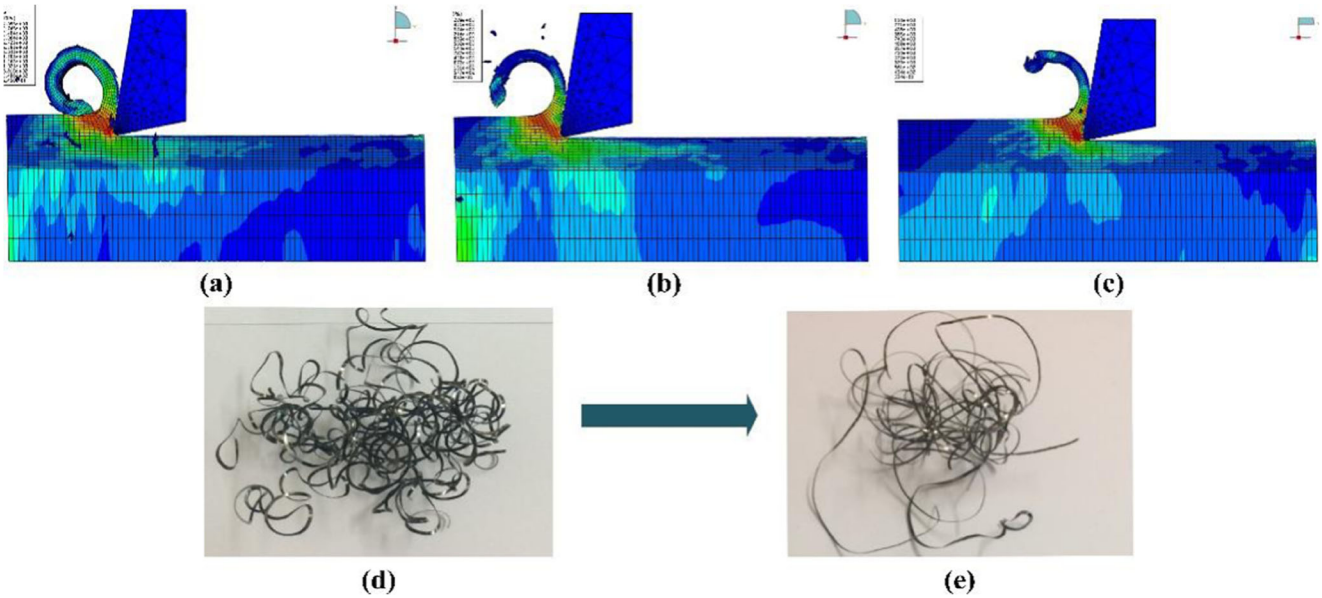

Fig. 22 Variation of chips morphology under different groove widths **a**, **d** 30; **b** 50; **c**, **e** 70 μm

two contacts respectively. The value of ρ_1 is the chip diameter and the value of ρ_2 is ∞ as the rake face of the turning tool is a plane. μ_1 and μ_2 are Poisson's ratio of two contacts respectively; E_1 and E_2 are elasticity modulus of two contacts respectively. According to Figs. 21 and 22, decrease of occupancy ratio of textures on rake face lead to the decrease of ρ_1. Consequently, with fixed F_n, μ_1, μ_2, E_1, and E_2, σ_c increases, which further indicates the increase of cutting force. Secondly, decrease of occupancy ratio of textures on rake face weakens the "secondary lubrication" effect. As a result, friction coefficient between the substrate and turning tool increases. Thirdly, decrease of occupancy ratio of textures on the rake face offers larger bond area between the substrate and turning tool, which is beneficial for the decrease of mechanical stress. In addition, increasing groove depth strengthens role of textures as a reservoir for cutting liquid and uniforms the distribution of lubrication film [27]. Hence, the "secondary lubrication" effect is reinforced and cutting performance of PG textured turning tool is promoted.

Apart from cutting force and friction coefficient, cutting performance of the PGT turning tool can also be evaluated from view of chips morphology. Figures 21, 22, and 23 indicate visualized theoretical and experimental chips morphology processed by the PGT turning tool with different dimensional parameters. Referring to the Figs. 18, 19, and 20, larger occupancy ratio of grooves on rake face and greater groove

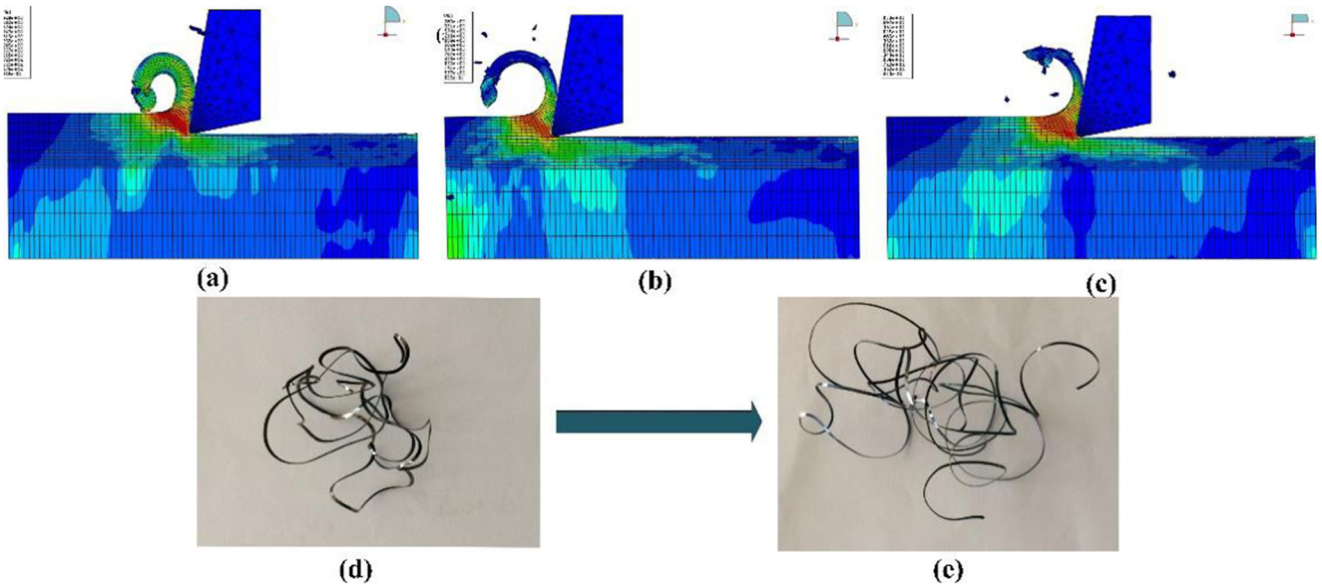

Fig. 23 Variation of chips morphology under different groove depths **a**, **d** 10; **b** 20; **c**, **e** 30 μm

depth generate lower cutting force and friction coefficient. Hence, smaller bending moment will be imposed on the chips. Larger occupancy ratio of grooves on rake face and greater groove depth also bring about larger thermal diffusion region and further prevent thermal accumulation [28]. Both of these effects yield the increase of chip diameter and decrease of chip thickness.

5 Conclusion

In this work, femtosecond laser is employed to fabricate microgrooves textures on the rake face of the cemented carbide YT15 turning tool for the promotion of cutting performance. The findings can be summarized as follows:

1. Moderate scanning velocity, lower laser fluence, and more scanning times are necessary for the absence of thermal incubation effect. Scanning gap of laser spot radius is appropriate for manufacturing microgrooves with optimized cross-sectional morphology.
2. Comparing with the NT turning tool, the employment of the PGT and VGT turning tools can significantly decrease cutting force and friction coefficient and the PGT turning tool is better for further application. But increase of cutting performance is accompanied by more severe tool wear as the tool strength is impaired with the existence of microgrooves
3. Increasing occupancy ratio and depth of microgrooves on rake face are beneficial for improving cutting performance of the PGT turning tool from aspects of cutting force, friction coefficient, and chips morphology.

Based on the achievements of this work, further work is still needed for the balance of cutting performance and tool wear.

Funding information This research is supported by the National High-tech R&D Program (863 Program) of China (No.2015AA042702), the National Science and Technology Major Project of China (No.2014ZX04001151), the and National Natural Science Foundation of China (No. 51275117).

References

1. Evans CJ, Bryan JB (1999) "Structured", "textured" or "engineered" surfaces. C Cirp Ann-Manuf Technol 48(2):541–556
2. Pettersson U, Jacobson S (2007) Textured surfaces for improved lubrication at high pressure and low sliding speed of roller/piston in hydraulic motors. Tribol Int 40(2):355–359
3. Sawada H, Kawahara K, Ninomiya T, Mori A, Kurosawa K (2004) Effect of precise periodic structures with femtosecond-laser on tribological characteristics under sliding tests. Int J Japan Soc Prec Eng 70(1):133–137
4. Marini M, Fontanari V, Bandini M, Benedetti M (2017) Surface layer modifications of micro-shot-peened Al-7075-T651: experiments and stochastic numerical simulations. Surf Coat Technol 321:265–278
5. Li Y, Deng JX, Chai YS, Fan WL (2016) Surface textures on cemented carbide cutting tools by micro EDM assisted with high-frequency vibration. Int J Adv Manuf Technol 82(9–12): 2157–2165
6. Wang XL, Kato K, Adachi K, Aizawa K (2003) Loads carrying capacity map for the surface texture design of SiC thrust bearing sliding in water. Tribol Int 36:189–197
7. Moshkovith A, Perfiliev V, Gindin D, Parkansky N, Boxman R, Rapoport L (2007) Surface texturing using pulsed air arc treatment. Wear 263:1467–1469
8. Mukherjee S, Dhara S, Saha P (2015) Enhancing the biocompatibility of Ti6Al4V implants by laser surface microtexturing: an in vitro study. Int J Adv Manuf Technol 76(1–4):5–15
9. Xu KC, Zhang C, Zhou R, Ji R, Hong MH (2016) Hybrid micro/nano-structure formation by angular laser texturing of Si surface for surface enhanced Raman scattering. Opt Express 24(10): 10352–10358
10. Lei ST, Devarajan S, Chang ZH (2009) A study of micropool lubricated cutting tool in machining of mild steel. J Mater Process Technol 209(3):1612–1620
11. Deng JX, Lian YS, Wu Z, Xing YQ (2013) Performance of femtosecond laser-textured cutting tools deposited with WS2 solid lubricant coatings. Surf Coat Technol 222:135–143
12. Kümmel J, Braun D, Gibmeier J, Schneider J, Greiner C, Schulze V, Wanner A (2015) Study on micro texturing of uncoated cemented carbide cutting tools for wear improvement and built-up edge stabilisation. J Mater Process Technol 215:62–70
13. Wang Z, Li YB, Bai F, Wang CW, Zhao QZ (2016) Angle-dependent lubricated tribological properties of stainless steel by femtosecond laser surface texturing. Opt Laser Technol 81:60–66
14. Ibatan T, Uddin MS, Chowdhury MAK (2015) Recent development on surface texturing in enhancing tribological performance of bearing sliders. Surf Coat Technol 272:102–120
15. Daoud M, Chatelain JF, Bouzid A (2015) Effect of rake angle on Johnson-Cook material constants and their impact on cutting process parameters of Al2024-T3 alloy machining simulation. Int J Adv Manuf Technol 81(9–12):1987–1997
16. Cheung E, Yuan W, Hua M (1999) Physical simulation of the deflection in turning of thin disk-shaped workpieces. Int J Adv Manuf Technol 15(12):863–868
17. Yang L, Ding Y, Wang M, Wang ML, Cao TT, Wang Y (2017) Numerical and experimental investigations on 342 nm femtosecond laser ablation of K24 superalloy. J Mater Process Technol 249:14–24
18. Kawasegi N, Sugimori H, Morimoto H, Morita N, Hori I (2009) Development of cutting tools with microscale and nanoscale textures to improve frictional behavior. Int J Precis Eng Manuf 33(3): 248–254
19. Wang WJ, Mei XS, Jiang GD (2009) Control of microstructure shape and morphology in femtosecond laser ablation of imprint rollers. Int J Adv Manuf Technol 41(5):504–512
20. Nolte S, Momma C, Jacobs H, Tünnermann A, Chichkov BN, Wellegehausen B, Welling H (1997) Ablation of metals by ultrashort laser pulses. JOSA B 14(10):2716–2722
21. Liu YJ, Li MZ, Ju FF (2017) Research on the process of flexible blank holder in multi-point forming for spherical surface parts. Int J Adv Manuf Technol 89(5–8):2315–2322
22. Zhang P, Kou SQ, Lin BJ, Wang YM (2015) Optimization for radial knurling connection process of assembled camshaft using response surface method. Int J Adv Manuf Technol 77(1–4):653–661
23. Kümmel J, Gibmeier J, Müller E, Schneider R, Schulze V, Wanner A (2014) Detailed analysis of microstructure of intentionally

formed built-up edges for improving wear behavior in dry metal cutting process of steel. Wear 311(1–2):21–30
24. Etsion I, Kligerman Y, Halperin G (1999) Analytical and experimental investigation of laser-textured mechanical seal faces. Tribol Trans 42:511–516
25. Yan P, Rong YM, Wang G (2016) The effect of cutting fluids applied in metal cutting process. Proc Inst Mech Eng B J Eng Manuf 230(1):19–37
26. Yang LJ, Ding Y, Cheng B, He JT, Wang GW, Wang Y (2018) Investigations on femtosecond laser modified micro-textured surface with anti-friction property on bearing steel GCr15. Appl Surf Sci 434:831–842
27. Kovalchenko A, Ajayi O, Erdemir A, Fenske G, Etsion I (2005) The effect of laser surface texturing on transitions in lubrication regimes during unidirectional sliding contact. Tribol Int 38(3): 219–225
28. Cohen G, Gilles P, Segonds S, Mousseigne M, Lagarrigue P (2012) Thermal and mechanical modeling during dry turning operations. Int J Adv Manuf Technol 58(1–4):133–140

Publisher's Note